2B-01

HOW ARE THE MELTING LAYER PROPERTIES ASSOCIATED WITH SNOW MICROPHYSICS? INSIGHTS FROM OBSERVATIONS OF MULTI-FREQUENCY RADARS AND A DUAL-POLARIZED RADAR

Haoran Li[1*] and Dmitri Moisseev[1,2]
1 Institute for Atmospheric and Earth System Research / Physics, Faculty of Science, University of Helsinki, Finland.
2 Finnish Meteorological Institute, Helsinki, Finland.

1. INTRODUCTION

In stratiform rainfall, the melting layer (ML) is often presented and can be identified as an enhanced reflectivity band, the so-called "bright band". Despite the debate on the exact microphysical processes that are taking place in the ML, both model simulations and observations have acknowledged that the radar-observed ML characteristics (e.g., enhancement of radar reflectivity, depth of the bright band and the "sagging" of the bright band) are influenced by the snow microphysics above it. There is, however, a lack of understanding on how the observed ML properties can reveal the associated snow microphysics.

This study is aiming to advance our understanding on the link between snow microphysical processes and ML properties. To achieve this, we utilize the unique synergic observations collected during Biogenic Aerosols Effects on Clouds and Climate (BAECC) from vertically pointing W-, Ka- and X-band radars and a coinciding dual-polarized C-band radar RHI scans. Additionally, surface precipitation snowfall observations are used to derive a method to diagnose snow riming fraction from dual-frequency Doppler radar observations. This method in combination with dual-polarization radar observations are used to characterize prevailing snow microphysical processes that take place above the ML.

2. MEASUREMENTS

The BAECC field campaign was carried out at the University of Helsinki Hyytiälä Station from February to September 2014 [Petäjä et al., 2016]. The vertically pointing X/Ka-band scanning Atmospheric Radiation Measurement (ARM) cloud radar (X/Ka-SACR) and marine W-band ARM cloud radar (MWACR) recorded the multi-frequency radar observations. A coinciding Finnish Meteorological Institute (FMI) C-band dual-polarization radar operated Range-Height Indicator (RHI) scans over Hyytiälä, providing the unique co-located observations for studying the stratiform precipitation. In this study, we use Z_{dr} and K_{dp} measurements observed by the FMI C-band radar. Details of the multi-frequency radar setup and FMI C-band radar can be found in (Kneifel et al., 2015) and (Li et al., 2018), respectively.

The calibration of X-SACR reflectivity is made by matching the simulated reflectivity from 2D-video disdrometer observations to the reflectivity observed at 500 m where the near-field effect is minimized (Sekelsky, 2002, Falconi et al., 2018). The gaseous attenuation is corrected by using the closest radio sounding as input to the millimeter-wave propagation model (Liebe, 1985) at all radar frequencies.

Microphysical properties of snowflakes were retrieved by combining observations from National Aeronautics and Space Administration Particle Imaging Package (PIP) and two OTT Pluvio^2 weighting gauges (von Lerber et al., 2017). Such retrievals were made from BAECC to the winter of 2018.

3. METHODS

In this study, we have implemented a ML-detection method using dual-polarized measurements. To examine the snow microphysical fingerprints on the ML, the riming fraction is introduced to separate unrimed and moderately/heavily rimed cases.

3.1 *Detection of the ML*

The detection of ML is based on radar reflectivity and polarimetric measurements. As discussed by Wolfensberger et al. (2016), the use of ρ_{hv} can underestimate the melting top. Thus, the local minimum of the X-SACR reflectivity gradient near the ρ_{hv}-detected ML top is identified as the melting top, which is similar with Wolfensberger et al. (2016). Instead of using ρ_{hv} to derive the melting base, we use linear depolarization ratio (LDR) observed by KaSACR, as the LDR signal is larger and needs much lower accuracy than ρ_{hv}.

3.2 *Diagnosing snow riming fraction*

We use rime mass fraction (FR), the ratio of accreted ice mass from the supercooled water to the total snowflake mass (Moisseev et al., 2017; Li et al., 2018), to classify unrimed and rimed snow. FR is defined as

$$FR = 1 - \frac{\sum_{n=1}^{\infty} N(D_n) m_{\mathrm{ur}}(D_n) \mathrm{d}D}{\sum_{n=1}^{\infty} N(D_n) m_{\mathrm{ob}}(D_n) \mathrm{d}D} \quad (1)$$

where $N(D_n)$ indicates the retrieved particle size distribution for the maximum particle diameter of D_n, m_{ur} and m_{ob} are the mass of unrimed and observed snowflakes, respectively. m_{ur} may be expressed by $m_{\mathrm{ur}} = 0.0053 D^{2.05}$ as shown by Moisseev et al. (2017) and Li et al. (2018).

* Corresponding author address: Haoran Li, INAR/ Physics, University of Helsinki, Helsinki, Finland; E-mail: haoran.li@helsinki.fi.

We use the algorithm developed by von Lerber et al. (2017) to retrieve the maximum particle diameter, particle size distribution, mass/velocity-size relation as well as precipitation rate (PR). Based on the scattering database of rimed snowflakes (Leinonen, & Moisseev, 2015; Leinonen & Szyrmer, 2015), the dual-wavelength ratio (DWR) between X- and Ka-bands and the Doppler velocity observed by X-SACR (V_X) can be derived. The impact of changing air density is mitigated by adjusting the air condition to 1000 hPa and 0℃ (Heymsfield et al., 2007).

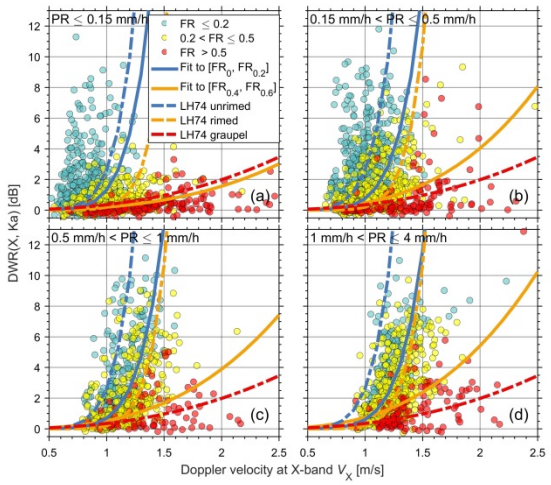

Figure 1. Scatter plot of DWR(X, Ka) vs. V_X (1000 hPa and 0 ℃) colored with FR. Mass-size and velocity-size relations from (Locatelli and Hobbs, 1974) are adopted for reference (dashed lines).

As shown in Figure 1, the scatterplot of DWR(X,Ka) and V_X shows significant dependence on FR. Power law fits for unrimed aggregates are applied to cases FR < 0.2 while the rimed cases are separated by 0.4 ≤ FR ≤ 0.6. The fit parameters are listed in the table below.

Table 1. Fitted parameters for DWR(X,Ka) = aV_X^b

Fitted parameters		a	b
LH74	Unrimed	2.6	7.3
	Rimed	0.2	9.8
	Graupel	0.35	2.5
PR ≤ 0.15 mm/h	Unrimed	1.3	7.3
	Rimed	0.2	2.96
0.15 mm/h < PR ≤ 0.5 mm/h	Unrimed	0.75	7.3
	Rimed	0.47	3.1
0.5 mm/h < PR ≤ 1 mm/h	Unrimed	0.69	7.3
	Rimed	0.52	2.9
1 mm/h < PR ≤ 4 mm/h	Unrimed	0.6	7.3
	Rimed	0.75	2.85

4. RESULTS

During BAECC, we have collected around 11 hour's observations of straitiform rainfall. As the time resolution for the FMI C-band radar RHI scan is 15 minutes, fewer profiles are identified to match with the multi-frequency radar measurements. For most cases the relative humidity (RH) around the ML top is < 95%. Thus, the effects of dry air infiltration, e.g., decreasing reflectivity, descending dual-polarization measurements, thinning the ML thickness (Carlin & Ryzhkov, 2019), should be minimized.

4.1 *Z_{dr} and K_{dp} profiles*

The Z_{dr} and K_{dp} profiles observed by FMI C-band radar are generalized by the ML top observed by the vertically pointing radars. Figure 2 shows the Z_{dr} and K_{dp} profiles grouped by PR. When PR ≤ 0.15 mm/h Z_{dr} is around 0.5 dB with no significant changes with height, while Z_{dr} decreases significantly as reaching the ML top when PR is larger. At the ML top, Z_{dr} is very close to 0 dB, indicating the formation of large fluffy aggregates. K_{dp} does not response to the snow above the ML when PR < 1 mm/h, while K_{dp} starts to increase at around 2700 m above the ML top when the precipitation is heavier.

4.2 *Saggy bright band*

Reflectivity profiles together with ρ_{hv} is presented in Figure 3. Generally, rimed cases are characterized by weaker bright band than unrimed, which is in line with the modeling study by Zawazki et al. (2005). Using polarimetric observations, Kumjian et al. (2016) found that riming can lead to the "sagging" of bright band in a case study. Our statistical observations show that riming seems leading to slightly more downward excursion of the reflectivity and ρ_{hv} when PR > 1. However, the minimum of ρ_{hv} is higher for rimed snow than unrimed when the precipitation is lighter.

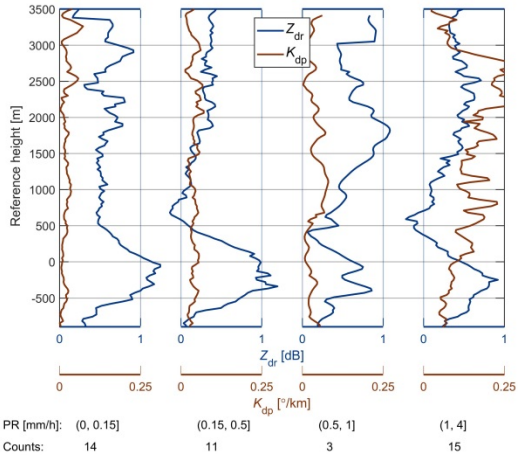

Figure 2. Generalized Zdr and Kdp profiles observed by FMI C-band radar with RHI scanning. The original profiles are shifted to let the ML top height (detected by X/Ka-SACR) reach 0 m. Namely, the reference height of 0 m

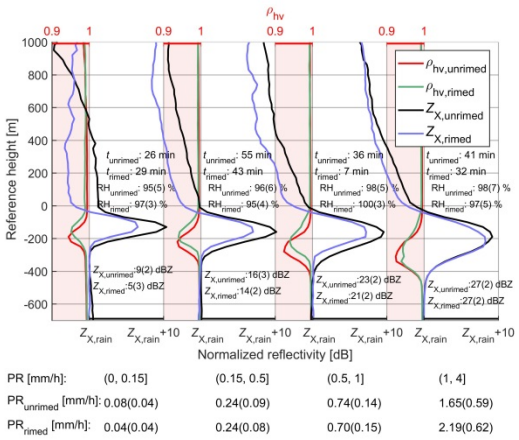

Figure 3. Normalized X-band radar profiles grouped by PR. Note that the profiles are shifted to let the ML top reach 0 m, and each reflectivity profile is normalized by offsetting the difference between $Z_{X,rain}$ and the median value of $Z_{X,rain}$ in the corresponding PR group. $t_{unrimed}$ and t_{rimed} indicate the total observing time in each group for unrimed and rimed cases, respectively. The median values of the X-band reflectivity at the ML bottom for unrimed $Z_{X,unrimed}$ and rimed $Z_{X,rimed}$ cases are marked just below the ML bottom with the standard values in brackets. The median and standard deviations (in brackets) of relative humidity (RH) at the ML top for unrimed ($RH_{unrimed}$) and rimed (RH_{rimed}) cases in each group are presented near the ML top. The median and standard deviations (in brackets) of PR for unrimed ($PR_{unrimed}$) and rimed (PR_{rimed}) cases in each group are presented in the lower part.

4.3 *Dark band*

The dark band is the decrease in the radar reflectivity near ML top (Kollias and Albrecht, 2005). For the spaceborne W-band radar, the observed dark band around the ML top may be due to the strong signal attenuation as discussed by Sassen et al. (2007). In this study, the dark band is identified as the decrease of radar reflectivity from above to the ML as shown by Sassen et al. (2005). Such dark band has also been called dim band by Heymsfield et al. (2008).

As shown in Figure 4, the decrease of W-band reflectivity starts as high as 1000 m above the ML. Such decrease is pronounced for unrimed and light precipitation cases, while no obvious dark band is found for rimed cases. Heymsfield et al. (2008) proposed that the formation of dark band at W-band above the ML is due to the change of particle size distribution during aggregation. The absence of dark band for rimed cases seems indicating that riming is associated with smaller particles, which is also supported by smaller DWR(X,Ka) of rimed cases above the ML (not shown).

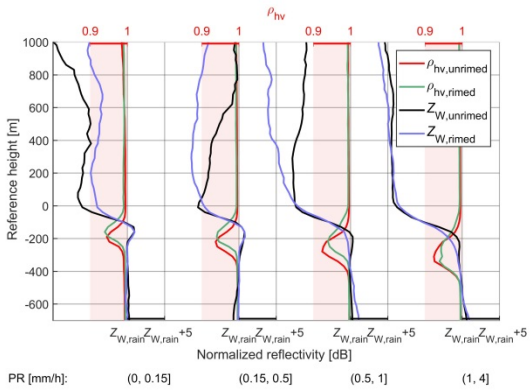

Figure 4. Same as Figure 3, but for the W-band radar. Note that the calibration of Ka-SACR is made by matching the reflectivity with X-SACR at cloud top, thus the attenuation from ML to above is not accounted.

5. CONCLUSIONS

In this study, we developed a method to classify unrimed and rimed snow based on DWR(X, Ka) and V_X. Statistical results show that,

1. Z_{dr} decreases to around 0 dB as approaching to the ML except for when PR < 0.15 mm/h where no significant change is found. K_{dp} is not sensitive to light precipitation while starts increasing at around 3000 m above the ML when PR > 1 mm/h.

2. Precipitation intensity has the strongest impact on ML properties. Increase in precipitation intensity causes bright band sagging.

3. Riming plays a secondary role on modulating the ML properties.

1) In moderate to heavy rainfall, riming causes additional bright band sagging. Riming does not seem to be linked to bright band sagging in light precipitation. The opposite effect is observed, i.e., unrimed cases are associated with the bright band sagging.

2) The radar reflectivity peak in ML at X-band is larger for lightly rimed cases than for heavily rimed ones when the non-Rayleigh effects are not significant.

3) Dark band is absent for rimed snow while it is pronounced when snowflakes are unrimed at light precipitation.

REFERENCES

Carlin, J. T., & Ryzhkov, A. V., 2019: Estimation of Melting Layer Cooling Rate from Dual-Polarization Radar: Spectral Bin Model Simulations. Journal of Applied Meteorology and Climatology, 58, 1485-1507.

Falconi, M. T., Lerber, A. V., Ori, D., Marzano, F. S., & Moisseev, D., 2018: Snowfall retrieval at X, Ka and W bands: consistency of backscattering and microphysical properties using BAECC ground-based measurements. Atmospheric Measurement Techniques, 11(5), 3059-3079.

Kneifel, S., Lerber, A., Tiira, J., Moisseev, D., Kollias, P., & Leinonen, J. 2015: Observed relations between snowfall microphysics and triple ‐ frequency radar measurements. Journal of Geophysical Research: Atmospheres, 120(12), 6034-6055.

Leinonen, J., & Moisseev, D., 2015: What do triple ‐ frequency radar signatures reveal about aggregate snowflakes?. Journal of Geophysical Research: Atmospheres, 120(1), 229-239.

Leinonen, J., & Szyrmer, W., 2015: Radar signatures of snowflake riming: A modeling study. Earth and Space Science, 2(8), 346-358.

Locatelli, J. D., & Hobbs, P. V., 1974: Fall speeds and masses of solid precipitation particles. Journal of Geophysical Research, 79(15), 2185-2197.

Heymsfield, A. J., Bansemer, A., and Twohy, C. H., 2007: Refinements to ice particle mass dimensional and terminal velocity relationships for ice clouds. Part I: Temperature dependence, Journal of the atmospheric sciences, 64, 1047–1067.

Heymsfield, A. J., Bansemer, A., Matrosov, S., & Tian, L., 2008: The 94 ‐ GHz radar dim band: Relevance to ice cloud properties and CloudSat. Geophysical Research Letters, 35(3), L03802.

Kollias, P., & Albrecht, B., 2005: Why the melting layer radar reflectivity is not bright at 94 GHz. Geophysical research letters, 32(24).

Kumjian, M. R., Mishra, S., Giangrande, S. E., Toto, T., Ryzhkov, A. V., & Bansemer, A., 2016: Polarimetric radar and aircraft observations of saggy bright bands during MC3E. Journal of Geophysical Research: Atmospheres, 121(7), 3584-3607.

Li, H., Moisseev, D., & von Lerber, A., 2018: How does riming affect dual ‐ polarization radar observations and snowflake shape?. Journal of Geophysical Research: Atmospheres, 123(11), 6070-6081.

Liebe, H. J., 1985: An updated model for millimeter wave propagation in moist air. Radio Science, 20(5), 1069-1089.

Moisseev, D., von Lerber, A., & Tiira, J., 2017: Quantifying the effect of riming on snowfall using ground ‐ based observations. Journal of Geophysical Research: Atmospheres, 122(7), 4019-4037.

Petäjä, T., O'Connor, E. J., Moisseev, D., Sinclair, V. A., Manninen, A. J., Väänänen, R., von Lerber, A., Thornton, J. A., Nicoll, K., Petersen, W., et al., 2016: BAECC: A field campaign to elucidate the impact of biogenic aerosols on clouds and climate, Bulletin of the American Meteorological Society, 97, 1909–1928.

Sassen, K., Campbell, J. R., Zhu, J., Kollias, P., Shupe, M., & Williams, C., 2005: Lidar and triple-wavelength Doppler radar measurements of the melting layer: A revised model for dark-and brightband phenomena. Journal of Applied Meteorology, 44(3), 301-312.

Sassen, K., Matrosov, S., & Campbell, J., 2007: CloudSat spaceborne 94 GHz radar bright bands in the melting layer: An attenuation ‐ driven upside ‐ down lidar analog. Geophysical Research Letters, 34(16).

Sekelsky, S. M., 2002: Near-field reflectivity and antenna boresight gain corrections for millimeter-wave atmospheric radars. Journal of Atmospheric and Oceanic Technology, 19(4), 468-477.

von Lerber, A., Moisseev, D., Bliven, L. F., Petersen, W., Harri, A. M., & Chandrasekar, V., 2017: Microphysical properties of snow and their link to Z e–S relations during BAECC 2014. Journal of Applied Meteorology and Climatology, 56(6), 1561-1582.

Wolfensberger, D., Scipion, D., & Berne, A., 2016: Detection and characterization of the melting layer based on polarimetric radar scans. Quarterly Journal of the Royal Meteorological Society, 142, 108-124.

Zawadzki, I., Szyrmer, W., Bell, C., & Fabry, F., 2005: Modeling of the melting layer. Part III: The density effect. Journal of the Atmospheric Sciences, 62(10), 3705-3723.